Regular Article

High-resolution brain tractography from X-ray phase-contrast images

Joshua Gobé[1], Hugo Rositi[2], Antoine Vacavant[3], Margaux Rivière[1], Chrystelle Po[4], Matthieu Chourrout[1],
Fabien Chauveau[1,a] (ORCID)

[1] Université Claude Bernard Lyon 1, Lyon Neuroscience Research Center, CNRS, INSERM, 69500 Bron, France
[2] LORIA, CNRS, Université de Lorraine, 54000 Nancy, France
[3] Université Clermont Auvergne, Clermont Auvergne INP, CNRS, Institut Pascal, 63000 Clermont-Ferrand, France
[4] Université de Strasbourg, CNRS, ICube UMR 7357, 67000 Strasbourg, France

Abstract X-ray phase contrast tomography (XPCT) can produce high contrast isotropic images of biological samples in only a few minutes thanks to the unique properties of the synchrotron X-ray beam. XPCT of brain tissue provides an exquisite contrast of white matter, which could be exploited for 3D directional analysis. In this article, we present the first XPCT-based pipeline to perform white matter tractography on rodent brains. We observed the disorganization of white matter in the vicinity of focal demyelinating lesions in the corpus callosum. The ability to obtain an isotropic, high-resolution tractogram is an important landmark which could drive further interest of the neuroscience community toward XPCT.

1 Introduction

White matter is a structure of the brain found in its deeper tissues implied in multiple physiological and cognitive processes. It is composed of bundles of axons, or nerve fibers. Axons are normally surrounded by myelin, a sheath of protein that helps conduct nerve impulses and protect the nerve fibers.

The study of white matter is of major importance as it can be altered or damaged by numerous brain diseases, ranging from stroke [1] to Alzheimer's [2] disease. As it is a complex 3-dimensional (3D) structure with fiber tracts presenting various orientations in space, the right tools are required to study it properly. However, the only customary ways currently at disposal to do so are diffusion-based magnetic resonance imaging (MRI) with specific acquisition methods (DTI [3], DSI [4], q-ball [5], etc.) and brain clearing coupled with light-sheet microscopy [6].

MRI-based techniques are broadly used thanks to their accessibility and ability to retrieve indirect information about fiber orientation as well as quantitative metrics which can act as biomarkers of axonal and myelin damage, both in vivo and ex vivo [7]. However, the modality shows a certain number of limits [8]. In vivo scans are bonded to low anisotropic resolution (typically $100\,\mu$m in a plane) due to biological and ethical constraints. Ex vivo scans can however reach higher and isotropic resolution (around $50\,\mu$m) at the cost of acquisition times potentially reaching more than 20 h for a single scan and the use of contrast agents or medium that can be problematic for the later use of other imaging modalities. Furthermore, the signal detected via diffusion MRI only conveys indirect and not specific information about myelinated fibers as it can be influenced by other tissues and microstructures such as non-neuronal cells, extracellular matrix, intracellular components [9]. Hence, it makes it difficult to assign specific pathological phenomenon outside of the major white matter pathways (corpus callosum, internal capsule, etc.) [10].

On the other hand, light-sheet microscopy after brain clearing allows an extremely fine resolution at the cost of a tedious chemical treatment of the sample over the course of several weeks. The removal of lipids inside the sample also makes it impossible to image later with another modality.

XPCT on the contrary can deliver 3D images of whole rodent brains with an isotropic resolution down to a few micrometers within a dozen minutes per sample after minimal chemical treatment to enhance the contrast. As the contrast comes from the various interfaces between different matters in the sample, it creates a strong distinction between structures that would otherwise appear very faintly with the use of absorption contrast (see Sect. 2.2). Especially, this technique makes the myelin appear in a strong hyper-signal when the sample has been dehydrated in more than 70% ethanol. Dehydration being the only chemical treatment applied to the

---

Matthieu Chourrout and Fabien Chauveau are Co-last authors.

a e-mail: chauveau@cermep.fr (corresponding author)

Table 1 Scan parameters for the different XPCT acquisitions

Species	Mouse	Rat
Beamline	ID19	ANATOMIX
Voxel size (isotropic) [μm]	7.5	5.5
Exposure time [s]	0.15	0.035
Number of projections	2000 (180°)	3600 (360°)
Peak energy [keV]	19	24
Sample-to-detector distance [m]	1	1.10

sample, the process is quick and reversible without damaging the sample; this way, further analysis can be performed with other imaging techniques.

From this observation, we set the goal to exploit this technique to perform a fiber tractography, similarly to what is done with MRI-based techniques since multiple decades and what has been achieved more recently with brain clearing [6].

Fiber tractography (FT) is a 3D reconstruction technique used to assess white matter tracts by simulating streamlines using image data. It consists in propagating a streamline from a seed by following the trajectory dictated by imaging data until a stopping criterion is met, it being usually an angle threshold assuming a turn too sharp makes the fiber become unrealistic, or a border of the white matter. If the algorithms are in themselves modality agnostic, only needing a map of local fiber orientation and a mask of white matter, FT was until recently exclusive to diffusion MRI because of the ease to obtain these two informations.

However, it has been shown that it is possible to retrieve fiber orientation information and a segmentation of the white matter from XPCT images [11]. In this article, we thus present a proof-of-concept tool to generate a tractography based on XPCT.

2 Materials and methods

2.1 Animals

All experimental procedures involving animals and their care were carried out in accordance with European regulations for animal use (EEC Council Directive 2010/63/EU, OJ L 276, Oct. 20, 2010). The study was approved by our local review board "Comité d'éthique pour l'Expérimentation Animale Neurosciences Lyon" (CELYNE—CNREEA Number: C2EA 42, APAFIS#7457-2016110414498389, 5892-2016063014207327, 187-2015011615386357). Mice and rats were housed in a temperature- and humidity-controlled environment (21 ± 3 °C), with 12:12 h light–dark cycle, with free access to standard chow and tap water. We used a pathological model of focal demyelination induced by stereotaxic, unilateral injection of lysophosphatidylcholine (LPC) in the corpus callosum, which has been previously described for the mouse in [11] and for the rat in [12].

2.2 Sample treatment

All animals were euthanized by intracardiac perfusion with phosphate-buffered saline (PBS) followed by formaldehyde 4%, and their brains were harvested. They were then fixed in formaldehyde 4% and then dehydrated in successive ethanol baths of increasing concentrations (30–50–70–96%). The total time for the preparation of a single sample was about 1 h, and multiple samples can be prepared simultaneously. Finally, the mouse samples were conditioned in 1 cm diameter plastic tubes filled with ethanol 96% and scanned in the same tubes and 2 cm diameter plastic tubes for rat samples.

2.3 Image acquisition

Imaging sessions were carried out at the ID19 beamline of the ESRF, the European Synchrotron (ESRF, Grenoble, France) for mouse brains. Rat brains were imaged at the ANATOMIX beamline at the SOLEIL facility (Saint-Aubin, France).

Phase-contrast imaging was performed thanks to the propagation-based technique, which exploits free-space propagation to detect interference fringes. The experiments were carried out with a "pink" incident X-ray beam generated by the undulator, allowing energies ranging from 19 to 35 keV. The scan parameters are listed in Table 1.

2.4 Image reconstruction and preprocessing

The images were reconstructed using Paganin algorithm implemented through the PyHST2 software [13] with a δ/β ratio of 1000 and exported as a volume in.raw format, then processed to get rid of ring artifacts with a licensed software developed by NOVITOM (Grenoble, France, 2022; https://www.novitom.com/en/). Brains were segmented from the background with the Thermo Scientific Amira Software version 2022.2 (Thermo Fisher Scientific; thermofisher.com), with a semi-manual threshold-based method, and finally exported as a.raw file.

2.5 Workstation

All computation tasks were performed on a Windows workstation with an Intel dual-core 2.30 GHz CPU, 512Go RAM and an NVIDIA Quadro p6000 GPU.

2.6 Language, libraries and softwares

The fiber orientation script is written in Python 3.9.7. It runs in a virtual environment with the numpy [14], scipy [15], numba [16] and nibabel [17] libraries. The napari library [18] can be used to easily open and visualize intermediate images saved in.npy format. White matter segmentation was performed with the IPSDK Explorer 3.2 (Reactiv'IP; Grenoble, France, 2022; https://www.reactivip.com/). Fiber tractography is performed using the Diffusion Toolkit software and visualization with TrackVis [19].

3 Results

3.1 Pipeline

For the tractography algorithm to work, it needs two files containing information derived from imaging data: one for the fiber orientation (vectorial map) and another for the tractography boundaries and seeds (white matter mask). We designed a pipeline that can generate these two files from the reconstructed and preprocessed XPCT images (Fig. 1).
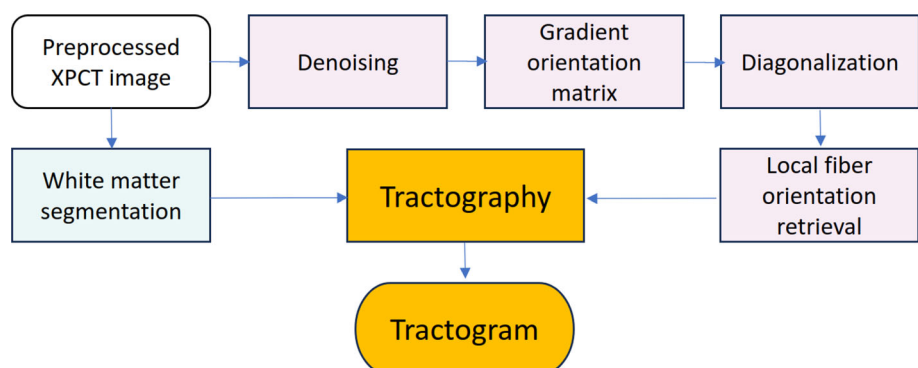
3.1.1 Fiber orientation

First, denoising of the preprocessed image is performed by convolution with a Gaussian kernel. The standard deviation of the denoising kernel must be carefully chosen so as not to make the smaller structures disappear while still smoothing the gray-level values within the fiber bundles. The value is to be fine-tuned manually according to the pixel size and the size of the structures in the sample. The impact of this parameter can clearly be observed in Fig. 2: omitting the denoising process leads to little to no coherent orientation retrieval outside the smallest tube-like structures (for example the striatum), whereas as value too large fails to assess those same structures while favoring the larger white matter tracts (such as the corpus callosum). Here, we settled on 1.2 for the mice and 2.0 for the rats.

We then compute the first order image intensity gradient of the denoised image for each voxel along the 3 spatial axes. This way, we can construct the gradient orientation matrix for each voxel by tensor product of the gradient vector by itself [11].

Diagonalization of the matrix reveals a new orthogonal base of space in which the eigenvector $\vec{v_1}$ associated with the largest eigenvalue λ_1 indicates the direction of the largest intensity variation [20]. In XPCT, the change in contrast is the result of an interface between two mediums. Following this idea, we can assume that $\vec{v_1}$ must correspond to the eigenvector normal to the interface. However, there are significant variations in the local morphology of the white matter in the sample: the fiber bundles we want to study are not always perfect tube-like structures and vary in radius. To assess the local fiber orientation, we must thus use a combination of the two remaining eigenvectors $\vec{v_2}$ and $\vec{v_3}$ (associated, respectively, with λ_2 and λ_3, given $\lambda_2 > \lambda_3$) instead of only considering $\vec{v_3}$ as the local orientation vector.

We assume the weight of each eigenvector depends on the local morphology of the structures, described by comparison of the eigenvalues (Fig. 3). In the case of small tube-like structures, $\vec{v_3}$ will be an accurate approximation of the local fiber orientation. However, the more plate-like structure becomes, the more the accuracy of the approximation declines.

Fig. 1 Schematic representation of the processing steps of tractography pipeline
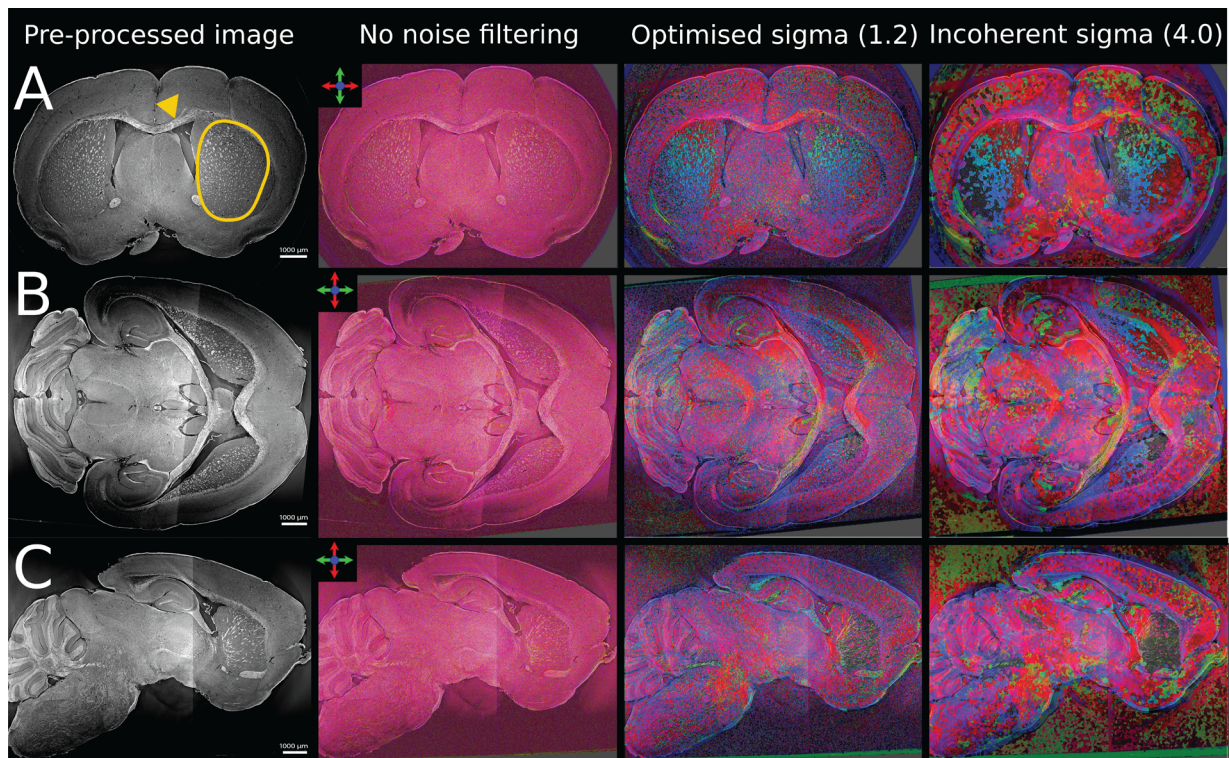
Fig. 2 Comparison of preprocessed data and color-coded orientation maps of a mouse brain obtained with the described fiber orientation algorithm superposed with the preprocessed image to highlight major white matter tracts. XYZ coordinates of the orientation vector are attributed, respectively, each channel of the RGB color space. A is coronal plane, B is axial plane, and C is sagittal plane. It can clearly be seen that without noise filtering, little to no correct orientation can be retrieved from the image, especially in larger fiber tracts like the corpus callosum (pointed with the arrowhead); with a standard deviation too high, the orientation becomes unrealistic around smaller fiber tracts, like for example in the striatum (circled). It should be noted that the sample was acquired by stitching two overlaping scans with a vertical translation in order to image the whole brain, which explains the jump in contrast visible on rows B and C; however, it does not have a significant impact on the output

Fig. 3 Comparison of eigenvalues provides local 3D morphological information about the structure of interest. λ_1, λ_2 and λ_3 are the eigenvalues corresponding to the eigenvectors v_1, v_2 and v_3, obtained by diagonalization of the orientation matrix

This way, we use Eq. (1) to define fiber orientation for each voxel taking into account the local morphology. We call $\vec{FO}$ the vector defining the fiber orientation of the voxel, λ_2 and λ_3 the smallest eigenvalues, $\vec{v_2}$ and $\vec{v_3}$ the eigenvectors associated with λ_2 and λ_3.

$$\vec{FO} = \frac{\lambda_3}{\lambda_2 + \lambda_3} \vec{v_2} + \frac{\lambda_2}{\lambda_2 + \lambda_3} \vec{v_3} \tag{1}$$

The fiber orientation map is finally converted into a NIfTI file constituting a valid input for the Diffusion ToolKit software.

3.1.2 White matter segmentation

In diffusion MRI, white matter segmentation is derived from orientation data by applying an arbitrary threshold to the fractional anisotropy (FA) map. In XPCT images, white matter is clearly visible and distinguishable from the other tissues [11]. Thus, we do

Fig. 4 Views of the corpus callosum of an LPC-injected mouse. A is the contralateral hemisphere, B is the ipsi-lateral hemisphere. 1 is preprocessed image; 2 is the binary mask generated with the random forest algorithm. The focal demyelination is circled on the ipsi-lateral hemisphere; the segmentation technique allows to accurately assess the demyelination
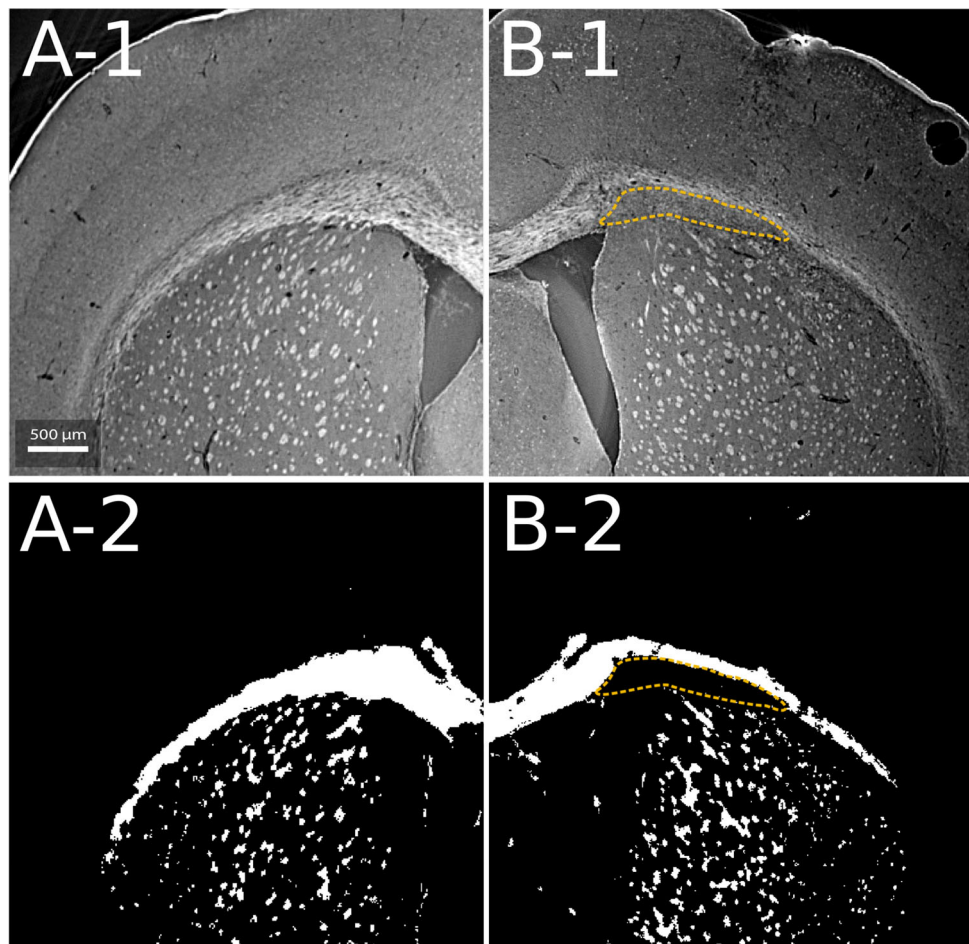
not have to resort to orientation data to identify it, which reduces the potential bias that would be caused by following strictly the traditional pipeline on different data.

We performed white matter segmentation via machine learning, using the random forest algorithm. The model was manually trained using the framework provided by the IPSDK Explorer software.

We used a multi-class strategy based on the size and morphology of the different structures of the white matter to optimize the accuracy of the model.

The model used 9 different types of features, both filters and morphology operations, with radius ranging from 1 to 5 pixels with a 3D structural element. The more decisive is variance, Gaussian filtering and morphological closing with the highest radius. The number of trees was set to 50.

Finally, all the classes are merged into one to create a binary mask of white matter (Fig. 4), and the volume is converted into a nifti file constituting a valid input for the Diffusion ToolKit software. This method succeeds in taking into account the area of demyelination by excluding it from the final mask while still providing an accurate delineation of the healthy white matter.

3.1.3 Tractography

The Diffusion Toolkit software was used to perform the fiber tractography with as inputs the two files described in Sects. 3.1.1 and 3.2.2. It uses a deterministic algorithm, and spline filtering at the end of the tractography to smoothen the generated fibers.

As the resolution of XPCT images is about 20 times higher, fibers are less likely to take sharp turns from one voxel to another. It allows for the reduction in the angular threshold compared to MRI. Here, we used a threshold of 30 degrees.

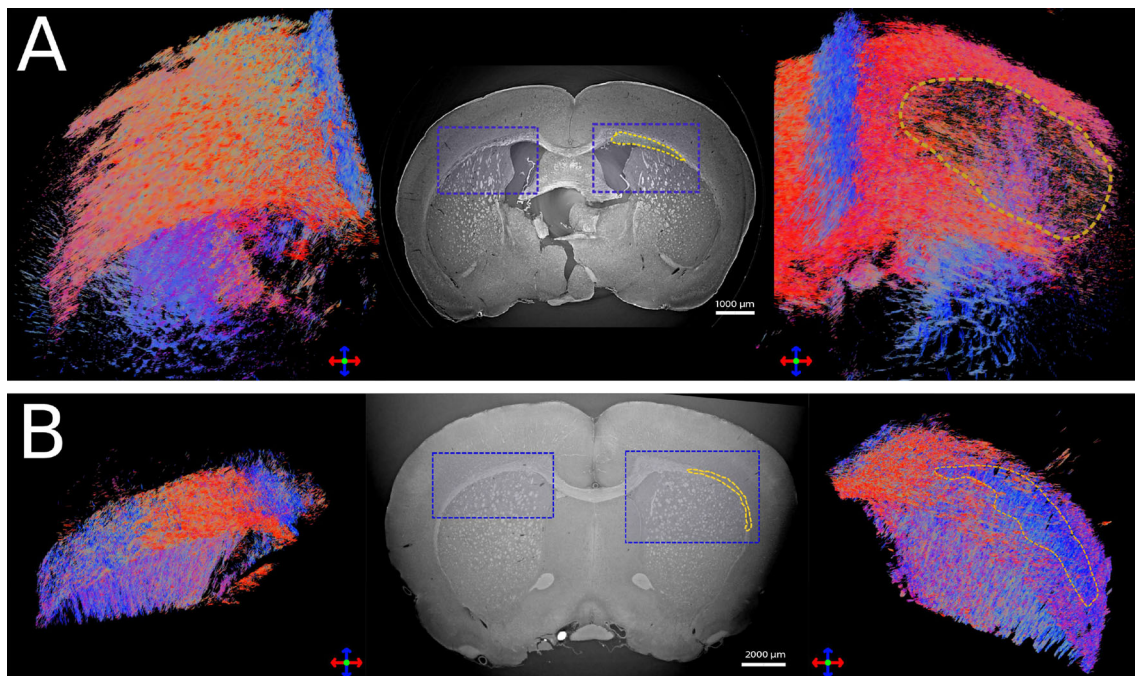The output file is a.trk file which we can open and handle with the TrackVis software, from the same suite.

Fig. 5 Comparison of tractograms of the corpus callosum for the contra-lateral (left) and ipsi-lateral (right) hemispheres. The color of the segments indicates the local orientation of the tracts as a combination of 3 channels: red are tracts along the axis normal to the saggital plane; blue, to the transverse plane; green, to the coronal plane. The focal demyelination is circled in yellow-dotted line on the preprocessed image (center) and on the tractograms, and the areas where tractography was performed are framed in blue. **A** Mouse brain; **B** rat brain
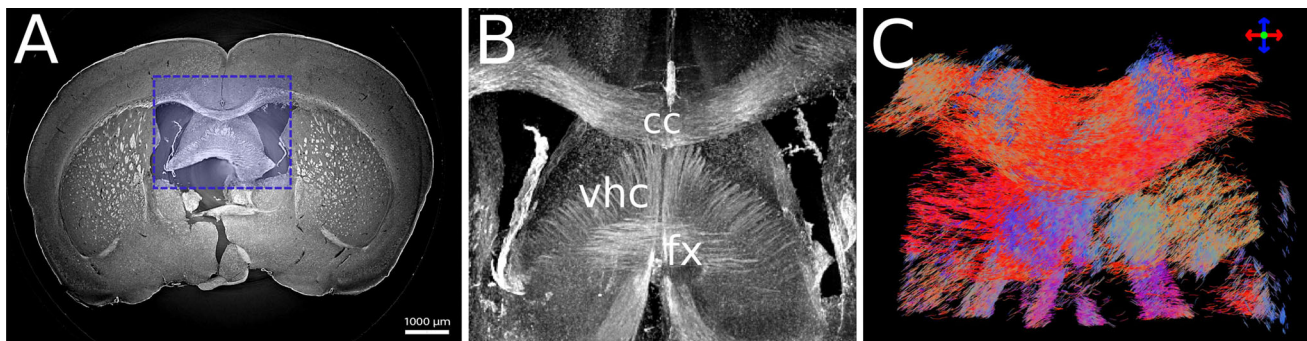

Fig. 6 Region of interest for fiber crossing in a mouse brain. **A** Preprocessed image; **B** maximum intensity projection (MIP) over 50 slices (325 μm) of the highlighted region of **A**. It represents the corpus callosum (cc), the ventral hippocampal commissure (vhc) and the fornix (fx). **C** generated tractography of the highlighted region

3.2 Tractograms

3.2.1 Assessing focal demyelination

We can assess pathological cases with the presented tractography pipeline, as shown in Fig. 5 for the case of local demyelination which is a model of multiple sclerosis.

The impact of the injection of LPC is clearly visible in the ipsi-lateral hemisphere: the sudden drop of fiber density can be assessed in the corpus callosum, whereas in the contralateral hemisphere, the integrity of the white matter is not visibly altered.

3.2.2 Fiber crossing

A major challenge concerning fiber tractography is to assess regions where multiple tracts of fibers cross each other (fiber crossings).

Figure 6 shows how the tractography pipeline deals with fiber crossing in the fornix, a region subjected to fiber crossing issues [21]. The tractogram shows fibers going in different directions coherently with what the maximum intensity projection (MIP) suggests

and allows to distinguish the two planes of fibers constituting the fiber crossing between the fornix and the ventral hippocampal commissure from each other. However, the simulated fibers are not as well defined as in the MIP.

4 Discussion

Multi-scale imaging tends to become more and more of a standard in biomedical research [22]: the different modalities do not compete but rather complete each other as they all convey useful but unique information. This is why we described a proof-of-concept pipeline to compute high-resolution fiber tractography from XPCT data. As we showed, fiber tractography algorithms are not modality-specific and can be used to process data acquired from other modalities. More than a new gold-standard for studying white matter tracts, we provide a framework in which every component is modular and subject to change and upgrade.

However, several issues can be addressed in the presented results. First of all, the generated fibers tend to be too short compared to what could be expected based on MRI tractography [21], which can be seen in Fig. 5. The pipeline also fails to tackle the narrowest fiber tracts for which the tractography becomes more imprecise as it can be seen in Fig. 6. These issues are most likely caused by the limits of the algorithms and methods used for both orientation retrieval and white matter segmentation. Retrieving orientation data from greyscale images (especially fiber orientation) is still an ongoing challenge, not only in neuroscience or biology but also in material science [23]. Updating the pipeline with more accurate algorithms will help resolve the issue concerning the coherence of the simulated fibers. This will allow to make the most of the tractogram format, by using for example fixel-based analysis [24]. In the same way, other strategies can be imagined to obtain a more robust segmentation of white matter, whether automatic or manual, with or without using machine learning or artificial intelligence.

From a more practical standpoint, there are also some restrictions originating from software involved in the pipeline. For convenience reasons, we used licensed software to perform the preprocessing of the data, but free alternatives exist for both eliminating ring artifacts [25] and segmentation of the brain [26], so that preprocessing the image won't be a limiting factor for the use of the pipeline. Open-source alternatives also exist for segmenting the white matter. The Diffusion Toolkit software has a size limit for the input files it takes of around 5 Gb. This currently restricts the pipeline to a local usage, but performing a tractography at the scale of the entire brain is theoretically possible.

XPCT is a modality allowing isotropic 3D data of unstained white matter at the micrometer scale, which makes it particularly relevant for usage in neuroscience. This way, a broad spectrum of applications could be tackled as a consequent number of brain pathologies impact the white matter to different extents: multiple sclerosis, stroke [1], Alzheimer's disease [2], etc. The simple and reversible dehydration of the sample also allows an effective "transpathological" approach [27]: the same samples can be imaged with different modalities prior and after the XPCT acquisitions, and particularly diffusion MRI which is among the most popular modalities to study white matter from a structural standpoint thanks to its easy access to fiber tractography. Because staining of the sample isn't needed, other structures are accessible with the same dataset, such as for example the vascular network [28]. Finally, important progress is also being made on the beamline installations, permitting routine scans of samples always increasing in size and thus no longer restricting XPCT usage in neuroscience to rodent models or small samples [29].

As for now, no reference method was used to assess the accuracy of the aforementioned pipeline as it is still a proof of concept and needs to be refined to be used in practical cases. However, several reference methods, such as histology [30], contrast-enhanced CT [31], and high-resolution diffusion-weighted imaging [32], could be used in future as ground truth to validate this tool.

5 Conclusion

In this work, we developed an image processing pipeline to perform white matter fiber tractography from synchrotron-radiation XPCT images. We described the modular framework we developed to achieve that goal as well as the different tools and algorithms we used to compute fiber orientation and white matter segmentation. This allowed us to perform fiber tractography of various regions of both mouse and rat brains. This way, we assessed the relevance of this technique to solve fiber crossings and evaluate the impact of focal demyelination in a pathological model. We found out the current pipeline opens promising possibilities, but more accurate algorithms could enhance the quality of the tractography and allow its usage in a broader range of pathological cases.

Author contributions JG was contributed to conceptualization, software, investigation, visualization, methodology, writing—original draft. HR was contributed to conceptualization, resources, software, supervision, writing—review and editing. AV was contributed to conceptualization, resources, software, writing—review and editing. MR was contributed to resources, investigation. CP was contributed to resources, writing—review and editing. MC was contributed to conceptualization, software, validation, investigation, visualization, methodology, writing—review and editing. FC was contributed to conceptualization, data duration, supervision, funding acquisition, investigation, writing—review and editing, project administration.

Data Availability Statement This manuscript has associated data in a data repository. [Authors' comment: The data that support the findings of this study are not openly available due to the size of the files but are fully available from the corresponding author upon request.]

References

1. S. Baltan, Stroke in CNS white matter: models and mechanisms 2019. Neurosci. Lett. **711**, 134411 (2019). https://doi.org/10.1016/j.neulet.2019.134411
2. S.E. Nasrabady, B. Rizvi, J.E. Goldman, A.M. Brickman, White matter changes in Alzheimer's disease: a focus on myelin and oligodendrocytes. Acta Neuropathol. Commun. **6**(1), 22 (2018). https://doi.org/10.1186/s40478-018-0515-3
3. L.J. O'Donnell, C.-F. Westin, An introduction to diffusion tensor image analysis. Neurosurg. Clinc. North Am. **22**(2), 185 (2011). https://doi.org/10.1016/j.nec.2010.12.004
4. Q. Tian, G. Yang, C.W.U. Leuze, A. Rokem, B.L. Edlow, J.A. McNab, Generalized diffusion spectrum magnetic resonance imaging (GDSI) for model-free reconstruction of the ensemble average propagator. NeuroImage **189**, 497–515 (2019). https://doi.org/10.1016/j.neuroimage.2019.01.038
5. D.S. Tuch, Q-ball imaging. Magn. Reson. Med. **52**(6), 1358–1372 (2004). https://doi.org/10.1002/mrm.20279
6. L. Ye, W.E. Allen, K.R. Thompson, Q. Tian, B. Hsueh, C. Ramakrishnan, A.-C. Wang, J.H. Jennings, A. Adhikari, C.H. Halpern, I.B. Witten, A.L. Barth, L. Luo, J.A. McNab, K. Deisseroth, Wiring and molecular features of prefrontal ensembles representing distinct experiences. Cell **165**(7), 1776–1788 (2016). https://doi.org/10.1016/j.cell.2016.05.010
7. J. Zhang, M. Aggarwal, S. Mori, Structural insights into the rodent CNS via diffusion tensor imaging. Trends Neurosci. **35**(7), 412–421 (2012). https://doi.org/10.1016/j.tins.2012.04.010
8. E. Calabrese, A. Badea, C.L. Coe, G.R. Lubach, M.A. Styner, G.A. Johnson, Investigating the tradeoffs between spatial resolution and diffusion sampling for brain mapping with diffusion tractography: Time well spent? Hum. Brain Mapp. **35**(11), 5667–5685 (2014). https://doi.org/10.1002/hbm.22578
9. M. Georgiadis, M. Menzel, J.A. Reuter, D.E. Born, S.R. Kovacevich, D. Alvarez, H.M. Taghavi, A. Schroeter, M. Rudin, Z. Gao, M. Guizar-Sicairos, T.M. Weiss, M. Axer, I. Rajkovic, M.M. Zeineh, Imaging crossing fibers in mouse, pig, monkey, and human brain using small-angle X-ray scattering. Acta Biomater. **164**, 317–331 (2023). https://doi.org/10.1016/j.actbio.2023.04.029
10. A. Yendiki, M. Aggarwal, M. Axer, A.F.D. Howard, A.-M.V.C. Van Walsum, S.N. Haber, Post mortem mapping of connectional anatomy for the validation of diffusion MRI. Neuroimage **256**, 119146 (2022). https://doi.org/10.1016/j.neuroimage.2022.119146
11. M. Chourrout, H. Rositi, E. Ong, V. Hubert, A. Paccalet, L. Foucault, A. Autret, B. Fayard, C. Olivier, R. Bolbos, F. Peyrin, C. Crola-da-Silva, D. Meyronet, O. Raineteau, H. Elleaume, E. Brun, F. Chauveau, M. Wiart, Brain virtual histology with X-ray phase-contrast tomography Part I: whole-brain myelin mapping in white-matter injury models. Biomed. Opt. Express **13**(3), 1620 (2022). https://doi.org/10.1364/BOE.438832
12. M. Zhang, G. Hugon, C. Bouillot, R. Bolbos, J.-B. Langlois, T. Billard, F. Bonnefoi, B. Li, L. Zimmer, F. Chauveau, Evaluation of myelin radiotracers in the lysolecithin rat model of focal demyelination: beware of pitfalls! Contrast Media Mol. Imaging **2019**, 9294586 (2019). https://doi.org/10.1155/2019/9294586
13. A. Mirone, E. Gouillart, E. Brun, P. Tafforeau, J. Kieffer, PyHST2: an hybrid distributed code for high speed tomographic reconstruction with iterative reconstruction and a priori knowledge capabilities. Nucl. Instrum. Methods Phys. Res. Sect. B: Beam Interact. Mater. Atoms **324**, 41–48 (2014). https://doi.org/10.1016/j.nimb.2013.09.030. arXiv:1306.1392 [cs, math]
14. C.R. Harris, K.J. Millman, S.J. Walt, R. Gommers, P. Virtanen, D. Cournapeau, E. Wieser, J. Taylor, S. Berg, N.J. Smith, R. Kern, M. Picus, S. Hoyer, M.H. Kerkwijk, M. Brett, A. Haldane, J.F. Río, M. Wiebe, P. Peterson, P. Gérard-Marchant, K. Sheppard, T. Reddy, W. Weckesser, H. Abbasi, C. Gohlke, T.E. Oliphant, Array programming with NumPy. Nature **585**(7825), 357–362 (2020). https://doi.org/10.1038/s41586-020-2649-2. Number: 7825 Publisher: Nature Publishing Group
15. P. Virtanen, R. Gommers, T.E. Oliphant, M. Haberland, T. Reddy, D. Cournapeau, E. Burovski, P. Peterson, W. Weckesser, J. Bright, S.J. Walt, M. Brett, J. Wilson, K.J. Millman, N. Mayorov, A.R.J. Nelson, E. Jones, R. Kern, E. Larson, C.J. Carey, I. Polat, Y. Feng, E.W. Moore, J. VanderPlas, D. Laxalde, J. Perktold, R. Cimrman, I. Henriksen, E.A. Quintero, C.R. Harris, A.M. Archibald, A.H. Ribeiro, F. Pedregosa, P. Mulbregt, SciPy 1.0: fundamental algorithms for scientific computing in Python. Nat. Methods **17**(3), 261–272 (2020) https://doi.org/10.1038/s41592-019-0686-2 . Number: 3 Publisher: Nature Publishing Group
16. S.K. Lam, A. Pitrou, S. Seibert, Numba: a LLVM-based Python JIT compiler, in *Proceedings of the Second Workshop on the LLVM Compiler Infrastructure in HPC. LLVM '15* (Association for Computing Machinery, New York 2015), pp. 1–6. https://doi.org/10.1145/2833157.2833162
17. M. Brett, C.J.Markiewicz, M. Hanke, M.-A. Côté, B. Cipollini, P. McCarthy, D. Jarecka, C.P. Cheng, Y.O. Halchenko, M. Cottaar, E. Larson, S. Ghosh, D. Wassermann, S. Gerhard, G.R. Lee, H.-T. Wang, E. Kastman, J. Kaczmarzyk, R. Guidotti, J. Daniel, O. Duek, A. Rokem, C. Madison, D. Papadopoulos Orfanos, A. Sólon, B. Moloney, F.C. Morency, M. Goncalves, Z. Baratz, R. Markello, C. Riddell, C. Burns, J. Millman, A. Gramfort, J. Leppäkangas, J.J.F. Bosch, R.D. Vincent, H. Braun, K. Subramaniam, A. Van, K.J. Gorgolewski, P.R. Raamana, J. Klug, B.N. Nichols, E.M. Baker, S. Hayashi, B. Pinsard, C. Haselgrove, M. Hymers, O. Esteban, S. Koudoro, F. Pérez-García, J. Dockès, N.N. Oosterhof, B. Amirbekian, I. Nimmo-Smith, L. Nguyen, S. Reddigari, S. St-Jean, E. Panfilov, E. Garyfallidis, G. Varoquaux, J.H. Legarreta, K.S. Hahn, L. Waller, O.P. Hinds, B. Fauber, J. Roberts, J.-B. Poline, J. Stutters, K. Jordan, M. Cieslak, M.E. Moreno, T. Hrnčiar, V. Haenel, Y. Schwartz, B.C. Darwin, B. Thirion, C. Gauthier, I. Solovey, I. Gonzalez, J. Palasubramaniam, J. Lecher, K. Leinweber, K. Raktivan, M. Calábková, P., Fischer, P. Gervais, P. Gadde, T. Ballinger, T. Roos, V.R. Reddam, freec84: nipy/nibabel: 5.0.0. Zenodo (2023). https://doi.org/10.5281/zenodo.7516526 . https://zenodo.org/record/7516526
18. N. Sofroniew, T. Lambert, K. Evans, J. Nunez-Iglesias, G. Bokota, P. Winston, G. Peña-Castellanos, K. Yamauchi, M. Bussonnier, D. Doncila Pop, A. Can Solak, Z. Liu, P. Wadhwa, A. Burt, G. Buckley, A. Sweet, L. Migas, V. Hilsenstein, L. Gaifas, J. Bragantini, J. Rodríguez-Guerra,H. Muñoz, J. Freeman, P. Boone, A. Lowe, C. Gohlke, L. Royer, A. PIERRÉ, H. Har-Gil, A. McGovern, napari: a multi-dimensional image viewer for Python. Zenodo (2022). https://doi.org/10.5281/ZENODO.3555620 . https://zenodo.org/record/3555620
19. R. Wang, T. Benner, A.G. Sorensen, V.J. Wedeen, Diffusion toolkit: a software package for diffusion imaging data processing and tractography, in *Proceedings of the International Society for Magnetic*, vol. 15, no. 3720. (2007)

20. A.F. Frangi, W.J. Niessen, K.L. Vincken, M.A. Viergever, Multiscale vessel enhancement filtering, in *Medical Image Computing and Computer-Assisted Intervention—MICCAI'98*, ed. W.M. Wells, A. Colchester, S. Delp, vol. 1496 (Springer, Berlin, Heidelberg, 1998), pp. 130–137. https://doi.org/10.1007/BFb0056195 . Series Title: Lecture Notes in Computer Science. http://link.springer.com/10.1007/BFb0056195

21. L.-A. Harsan, C. Dávid, M. Reisert, S. Schnell, J. Hennig, D. Von Elverfeldt, J.F. Staiger, Mapping remodeling of thalamocortical projections in the living *reeler* mouse brain by diffusion tractography. Proc. Natl. Acad. Sci. (2013). https://doi.org/10.1073/pnas.1218330110

22. M. Phelps, M. Schwaiger, A. Chiti, Multi-scale imaging as an essential tool for precision medicine. Eur. J. Nucl. Med. Mol. Imaging **48**(8), 2319 (2021). https://doi.org/10.1007/s00259-021-05367-3

23. R. Rezakhaniha, A. Agianniotis, J.T.C. Schrauwen, A. Griffa, D. Sage, C.V.C. Bouten, F.N. Vosse, M. Unser, N. Stergiopulos, Experimental investigation of collagen waviness and orientation in the arterial adventitia using confocal laser scanning microscopy. Biomech. Model. Mechanobiol. **11**(3), 461–473 (2012). https://doi.org/10.1007/s10237-011-0325-z

24. T. Dhollander, A. Clemente, M. Singh, F. Boonstra, O. Civier, J.D. Duque, N. Egorova, P. Enticott, I. Fuelscher, S. Gajamange, S. Genc, E. Gottlieb, C. Hyde, P. Imms, C. Kelly, M. Kirkovski, S. Kolbe, X. Liang, A. Malhotra, R. Mito, G. Poudel, T.J. Silk, D.N., Vaughan, J. Zanin, D. Raffelt, K. Caeyenberghs, fixel-based analysis of diffusion mri: methods, applications, challenges and opportunities. NeuroImage **241**, 118417 (2021). https://doi.org/10.1016/j.neuroimage.2021.118417

25. N.T. Vo, R.C. Atwood, M. Drakopoulos, Superior techniques for eliminating ring artifacts in X-ray micro-tomography. Opt. Express **26**(22), 28396–28412 (2018). https://doi.org/10.1364/OE.26.028396. Publisher: Optica Publishing Group

26. Comet Technologies Canada Inc., C. Montreal: Dragonfly 2022.2 [Computer software]; software available at https://www.theobjects.com/dragonfly

27. M. Tian, X. He, C. Jin, X. He, S. Wu, R. Zhou, X. Zhang, K. Zhang, W. Gu, J. Wang, H. Zhang, Transpathology: molecular imaging-based pathology. Eur. J. Nucl. Med. Mol. Imaging **48**(8), 2338–2350 (2021). https://doi.org/10.1007/s00259-021-05234-1

28. L. Massimi, M. Fratini, I. Bukreeva, F. Brun, A. Mittone, G. Campi, R. Spanò, M. Mastrogiacomo, N.K. De Rosbo, A. Bravin, A. Uccelli, A. Cedola, Characterization of mouse spinal cord vascular network by means of synchrotron radiation X-ray phase contrast tomography. Physica Med. **32**(12), 1779–1784 (2016). https://doi.org/10.1016/j.ejmp.2016.09.015

29. P. Tafforeau, C. Walsh, W.L. Wagner, J. Daniyal A. Jafree, Bellier, C. Werlein, M.P. Kühnel, E. Boller, S. Walker-Samuel, J.L. Robertus, D.A. Long, J. Jacob, S. Marussi, N. Eeline Brown Holroyd, D.D. Jonigk, M. Ackermann, P.D. Lee, Complete brain from the body donor LADAF-2020-31. European Synchrotron Radiation Facility (2021). https://doi.org/10.15151/ESRF-DC-572252655

30. M.D. Budde, J.A. Frank, Examining brain microstructure using structure tensor analysis of histological sections. Neuroimage **63**(1), 1–10 (2012). https://doi.org/10.1016/j.neuroimage.2012.06.042

31. R. Mizutani, R. Saiga, M. Ohtsuka, H. Miura, M. Hoshino, A. Takeuchi, K. Uesugi, Three-dimensional X-ray visualization of axonal tracts in mouse brain hemisphere. Sci. Rep. **6**(1), 35061 (2016). https://doi.org/10.1038/srep35061. Publisher: Nature Publishing Group

32. G.A. Johnson, Y. Tian, D.G. Ashbrook, G.P. Cofer, J.J. Cook, J.C. Gee, A. Hall, K. Hornburg, C.C. Kaczorowski, Y. Qi, F.-C. Yeh, N. Wang, L.E. White, R.W. Williams, Merged magnetic resonance and light sheet microscopy of the whole mouse brain. Proc. Natl. Acad. Sci. **120**(17), 2218617120 (2023). https://doi.org/10.1073/pnas.2218617120. Publisher: Proceedings of the National Academy of Sciences

Springer